
Polarons in colossal magnetoresistive and high-temperature superconducting materials

Guo-meng Zhao

Department of Physics and Astronomy, California State University, Los Angeles,
CA 90032, gzhao2@calstatela.edu

We review some unconventional oxygen-isotope effects in colossal magnetoresistive manganites and high temperature superconducting cuprates to assess the role of electron-phonon coupling in the basic physics of these materials. These include the unconventional oxygen-isotope effects on the Curie temperature and electrical transport in doped ferromagnetic manganites, on the supercarrier mass of superconducting cuprates, and on the antiferromagnetic ordering temperature of undoped parent cuprates. These unconventional isotope effects clearly demonstrate that the formation of polarons/bipolarons due to strong electron-phonon coupling is relevant to the basic physics of these materials and may be important for the occurrence of colossal magnetoresistance and high-temperature superconductivity. We also identify the phonon modes that are strongly coupled to conduction electrons from the angle-resolved photoemission spectroscopy, tunneling spectra, and optical data of doped cuprates. We consistently show a strong electron-phonon coupling feature at about 20 meV along the antinodal direction, which should also be important to the pairing mechanism of high-temperature superconductivity.

1 Introduction

Over the last decades, very interesting phenomena such as high-temperature superconductivity and colossal magnetoresistance have been discovered in several doped perovskite oxides (e.g., cuprates [1] and manganites [2]). These doped oxides are characterized by strong electron-phonon interactions, significant carrier densities ($\geq 10^{21} \text{ cm}^{-3}$), and low mobility of the order or even less than the Mott-Ioffe-Regel limit ($ea^2/\hbar \sim 1 \text{ cm}^2/\text{Vs}$) (where a is the lattice constant). The very nature of the low-temperature ‘metallic’ state of these materials cannot be understood within the framework of the canonical theory of metals where electron-phonon coupling is rather weak and the Fermi energy is much larger than a characteristic phonon energy. Since the electron-phonon

interactions in these perovskite oxides are much stronger than in normal metals, new theoretical approaches based on the formation of polarons/bipolarons are required to understand the basic physics of these materials.

The concept of polarons was first introduced by Landau in 1933 [3]. If an electron is placed into the conduction band of an ionic crystal, the electron is “trapped by digging its own hole” due to a strong Coulombic interaction of the electron with its surrounding positive ions. The electron together with the lattice distortions induced by itself is called polaron (lattice polaron). Lattice polarons are not ‘bare’ charge carriers, but are the carriers which are dressed by lattice distortions. Later on, the polaron problem was treated in great detail. One of the examples is the Holstein’s treatment where an electron is trapped by self induced deformation of two-atomic molecules (Holstein polaron) [4, 5]. In this case, the polaron moves by thermally activated hopping at high temperatures with a diffusion coefficient $\omega a^2 \exp[-(E_p/2 - t)/k_B T]$, where ω is the vibration frequency, E_p is the polaron binding energy, and t is the bare hopping integral. Further extensive theoretical studies (for review see [6, 7]) have shown that polarons behave like heavy particles, and can be mobile with metallic conduction at sufficiently low temperatures. Under certain conditions [8] they form a polaronic Fermi liquid with some properties being very different from ordinary metals.

It is well known that electrons can change their mass in solids due to the interactions with ions, spins, and themselves. The renormalized (effective) mass of electrons is independent of the ion mass M in ordinary metals where the Migdal adiabatic approximation is believed to be valid. However, the effective mass of polarons m^* will depend on M . This is because the polaron mass $m^* = m \exp(\gamma E_p/\hbar\omega)$ [6, 9], where m is the band mass in the absence of the electron-phonon interaction, γ is a constant, and ω is a characteristic phonon frequency which depends on the masses of ions. Hence, there is a large isotope effect on the polaronic carrier mass, in contrast to the zero isotope effect on the effective carrier mass in ordinary metals.

The total exponent of the isotope effect on the effective carrier mass is defined as $\beta = \sum -d \ln m^*/d \ln M_i$ (M_i is the mass of the i th atom in a unit cell). For polaronic carriers, this definition leads to

$$\beta = -\frac{1}{2} \ln(m^*/m). \quad (1)$$

It is interesting that the simple relation $m^* = m \exp(\gamma E_p/\hbar\omega)$ is even valid in the weak coupling region in the case of the long-range Fröhlich electron-phonon interaction [9]. Then the polaron mass enhancement factor m^*/m in this case is simply equal to $\exp(-2\beta)$.

Therefore, if electron-phonon coupling in a solid is strong enough to form polarons and/or bipolarons, one will expect a substantial isotope effect on the effective mass of carriers. In this article, we will review some unconventional oxygen-isotope effects in both manganites and cuprates. These include oxygen-isotope effects on the Curie temperature and electrical trans-

port in doped ferromagnetic manganites, on the supercarrier mass of superconducting cuprates, and on the antiferromagnetic ordering temperature of undoped parent cuprates. The observed large unconventional isotope effects clearly demonstrate that the formation of polarons/bipolarons due to strong electron-phonon coupling is relevant to the basic physics of these materials and may be important for the occurrence of colossal magnetoresistance and high-temperature superconductivity.

2 Polarons in manganites

Doped manganites $\text{Ln}_{1-x}\text{A}_x\text{MnO}_3$ (where Ln is a trivalent rare earth ion and A is a divalent ion) have been found to exhibit some remarkable features. The undoped parent compound LaMnO_3 (with Mn^{3+}) is an insulating antiferromagnet [10]. When Mn^{4+} ions are introduced by substituting a divalent ion (e.g., Ca) for La^{3+} , the materials undergo a transition from a high-temperature paramagnetic and insulating state to a ferromagnetic and metallic ground state for $0.2 \leq x \leq 0.5$ [11]. For $0.5 \leq x \leq 0.8$, the materials exhibit an insulating, charge-ordered and antiferromagnetic ground state. The temperature at which the insulator-metal transition occurs can be increased by applying a magnetic field. As a result, the electrical resistance of the material can be decreased by a factor of 1000 or more [2], if the temperature is held in the region of the transition. This phenomenon is now known as colossal magnetoresistance (CMR).

The physics of manganites has primarily been described by the double-exchange model [12, 13]. Crystal fields split the Mn 3d orbitals into three localized t_{2g} orbitals, and two higher energy e_g orbitals which are hybridized with the oxygen p orbitals. Each manganese ion has a core spin of $S = 3/2$, and a fraction $(1 - x)$ have extra electrons in the e_g orbitals with spin parallel to the core spin due to strong Hund's exchange. The electron can hop to an adjacent Mn site with unoccupied e_g orbitals without loss of spin polarization, but with an energy penalty that varies with the angle between the core spins. This double-exchange model accounts qualitatively for ferromagnetic ordering and carrier mobility that depends on the relative orientation of Mn moments which near T_C will therefore be strongly dependent on the applied field. However, Millis, Littlewood and Shraiman [14] have pointed out that double-exchange alone cannot fully explain the data of $\text{La}_{1-x}\text{Sr}_x\text{MnO}_3$. They suggest that lattice-polaronic effects due to strong electron-phonon coupling (arising from a strong Jahn-Teller effect) should be involved. The basic argument [15] is that in the high-temperature paramagnetic state the electron-phonon coupling constant λ is large and the carriers are polarons, while the growing ferromagnetic order increases the bandwidth and thus decrease λ sufficiently for metallic behavior to occur below the Curie temperature T_C . On the other hand, Alexandrov and Bratkovsky [16] show that, in order to explain

CMR quantitatively, one needs to consider the formation of small bipolarons (pairs of small polarons) in the paramagnetic state.

Although it is generally accepted that a strong electron-phonon interaction plays an important role in the basic physics of manganites [17], a quantitative explanation of the CMR is lacking. The very nature of charge carriers in the ferromagnetic metallic state and in the paramagnetic state is still under intensive debate [14, 15, 16]. Moreover, electron-energy-loss (EELS) [18], and O 1s x-ray absorption spectroscopy [19] consistently show that doped holes in manganites are of oxygen p character as expected for doped charge-transfer insulators. This would raise a question of whether the double-exchange mechanism is still valid in doped charge-transfer insulators [20]. Thus, the present understanding of the physics in manganites is far from complete, and further theoretical and experimental studies are essential.

2.1 Giant oxygen-isotope shift of the Curie temperature

A first observation of the oxygen isotope effect on the Curie temperature was made in $\text{La}_{1-x}\text{Sr}_x\text{MnO}_{3+y}$ system by Zhao and Morris in 1995 [21]. In Fig. 1, the normalized magnetizations for the ^{16}O and ^{18}O samples of $\text{La}_{0.9}\text{Sr}_{0.1}\text{MnO}_{3+y}$ are plotted as a function of temperature. The oxygen isotope shifts of T_C were determined from the differences between the midpoint temperatures on the transition curves of the ^{16}O and ^{18}O samples. It is clear that the ^{18}O sample has a lower T_C than the ^{16}O sample by ~ 6.7 K. It should be noted that since the value of y is substantial (> 0.05) when samples are prepared below 1100 °C, the curie temperatures in these samples are much higher than that for the corresponding single crystal samples where y is close to zero. Actually the extra oxygen in the above chemical formula is caused by the existence of cation vacancies.

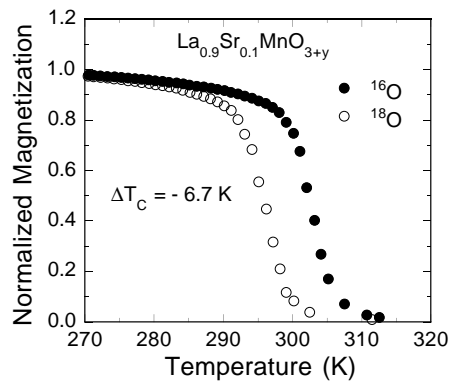


Fig. 1. Oxygen isotope effect on the Curie temperature of $\text{La}_{0.9}\text{Sr}_{0.1}\text{MnO}_{3+y}$. The figure is reproduced from Ref. [21].

On the other hand, the oxygen-isotope shift of T_C in $\text{La}_{0.8}\text{Ca}_{0.2}\text{MnO}_{3+y}$ is very large [22], as seen from Fig. 2. The samples with the same isotope mass have the same T_C , while the samples with a heavier oxygen isotope mass (about 95% of ^{18}O) have a much lower T_C . The relative isotope shift of T_C is as large as 10%. Such a large oxygen isotope shift of the ferromagnetic transition is very unusual since lattice vibrations were believed to play no role in the magnetic interactions of most magnetic materials. It is a clear-cut experiment to establish what many have suspected that atomic motion must be included in any viable description of the manganites [14]. It was also the first experiment in condensed matter physics to demonstrate that there can be a giant isotope shift of a magnetic transition temperature. The oxygen

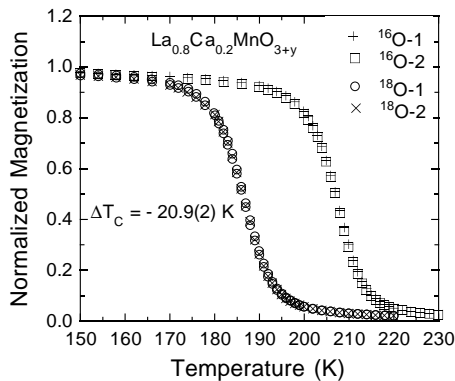


Fig. 2. Oxygen isotope effect on the Curie temperature of $\text{La}_{0.8}\text{Ca}_{0.2}\text{MnO}_{3+y}$. The figure is reproduced from Ref. [22].

isotope exponent is defined as usual, $\alpha_O = -(\Delta T_C/T_C)/(\Delta M_O/M_O)$, where both T_C and the oxygen isotope mass M_O are referred to a ^{16}O sample. With this definition, we obtain $\alpha_O = 0.85$ for $\text{La}_{0.8}\text{Ca}_{0.2}\text{MnO}_{3+y}$ and 0.142 for $\text{La}_{0.9}\text{Sr}_{0.1}\text{MnO}_{3+y}$.

The oxygen isotope effect on the Curie temperature has also been studied in other manganite systems [23, 24, 25]. It is found that [25] the α_O value increases rapidly as the Curie temperature decreases. In Fig. 3, we plot α_O vs the Curie temperature of ^{16}O samples. The data can be well fit by an equation

$$\alpha_O = 21.9 \exp(-0.016T_C). \quad (2)$$

The above simple empirical relation between α_O and T_C is quite unexpected. From a simple argument based on the double-exchange model and the small polaron theory discussed above, one would expect that [22] $T_C \propto \exp(-2\alpha_O)$. At least this scenario cannot quantitatively explain Eq. 2 possibly because it is too simple.

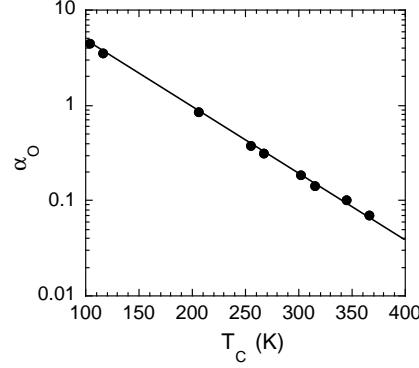


Fig. 3. α_O vs the Curie temperature of ^{16}O samples. The data are from Ref. [25].

It is also interesting that Eq. 2 is very similar to the relation between the pressure effect ($d \ln T_C / dP$) and T_C . Plotted in Fig. 4 is $d \ln T_C / dP$ (for fixed $x = 0.3$) as a function of T_C . The data can also be well fit by an equation

$$d \ln T_C / dP = 4.4 \exp(-0.016 T_C). \quad (3)$$

Combining Eq. 2 and Eq. 3, one has $\alpha_O = 5.0 d \ln T_C / dP$. Such a simple relation between the oxygen isotope exponent and the pressure effect implies that the oxygen isotope and pressure effects have the same origin, and that the observed oxygen isotope effect must be intrinsic.

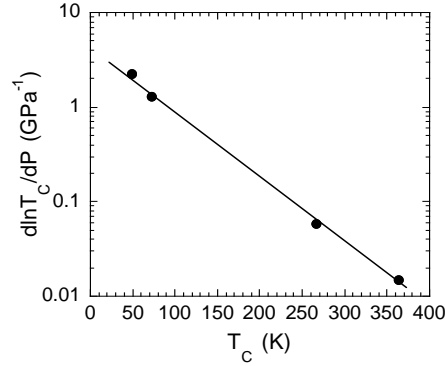


Fig. 4. $d \ln T_C / dP$ vs Curie temperature. The quantity $d \ln T_C / dP$ is referred to the pressure effect in the low pressure region. The figure is reproduced from Ref. [23].

2.2 Oxygen-isotope effects on electrical transport below the Curie temperature

The very nature of charge carriers and the electrical transport mechanism in the low-temperature metallic state of doped manganites have not been fully understood. At low temperatures, a dominant T^2 contribution in resistivity is generally observed, and has been ascribed to electron-electron scattering [26]. In contrast, Jaime *et al.* [27] have shown that the resistivity is essentially temperature independent below 20 K and exhibits a strong T^2 dependence above 50 K. They proposed single magnon scattering with a cutoff at long wavelengths to explain their data. In their scenario [27], they considered a case where the manganese e_g minority (spin-up) band lies slightly above the Fermi level (in the majority spin-down band) with a small energy gap of about 1 meV. This is in contradiction with the optical data [28] which show that the minimum band gap between the e_g minority and majority bands is even larger than 0.5 eV and that the size of the gap strongly depends on the chemical pressure. Alternatively, Zhao *et al.* [29] have recently shown that the temperature dependent part of the resistivity at low temperatures is mainly due to scattering by a soft optical phonon mode.

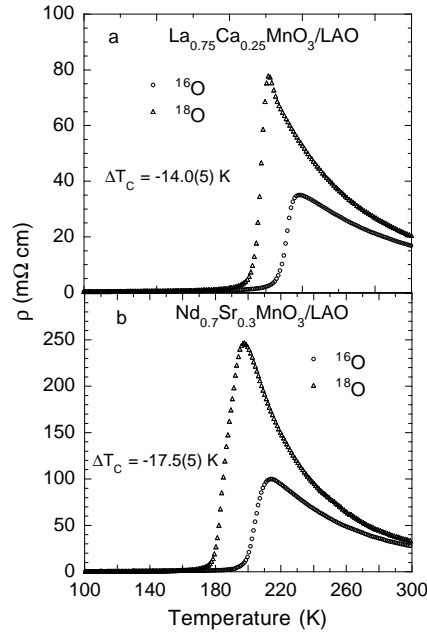


Fig. 5. The resistivity of the oxygen-isotope exchanged films of (a) $\text{La}_{0.75}\text{Ca}_{0.25}\text{MnO}_3$; (b) $\text{Nd}_{0.7}\text{Sr}_{0.3}\text{MnO}_3$. After Ref. [31].

Various CMR theories [14, 30, 16] predict different natures of charge carriers in the ferromagnetic state. In a theory by Alexandrov and Bratkovsky [16], polarons are considered as the carriers even in the low-temperature metallic state, while others [14, 30] believe that polaronic effects are not important at low temperatures. The clarification of the nature of charge carriers in the ferromagnetic state can discriminate those theoretical models. One of the effective and direct ways to prove or disprove the existence of polaronic carriers is to study the isotope effect on the effective carrier mass. This is because the polaron mass depend strongly on the isotope mass.

The oxygen-isotope effect on the intrinsic low-temperature resistivity has been studied [31] in high-quality epitaxial thin films of $\text{La}_{0.75}\text{Ca}_{0.25}\text{MnO}_3$ and $\text{Nd}_{0.7}\text{Sr}_{0.3}\text{MnO}_3$. The residual resistivity of these compounds shows a strong dependence on the oxygen-isotope mass. The quantitative data analyses suggest that the nature of the charge carriers in the ferromagnetic state of doped manganites are intermediate-size polarons.

Fig. 5 shows the resistivity of the oxygen-isotope exchanged films of $\text{La}_{0.75}\text{Ca}_{0.25}\text{MnO}_3$ (LCMO) and $\text{Nd}_{0.7}\text{Sr}_{0.3}\text{MnO}_3$ (NSMO) over 100-300 K. It is apparent that the ^{18}O samples have lower metal-insulator crossover temperatures and much sharper resistivity drop. The Curie temperature T_C normally coincides with a temperature where $d \ln \rho / dT$ exhibits a maximum. We find that the oxygen-isotope shift of T_C is 14.0(6) K for LCMO, and 17.5(6) K for NSMO, in excellent agreement with the results for the bulk samples [25].

In Fig. 6 we plot the low-temperature resistivity of the oxygen-isotope exchanged films of (a) LCMO; (b) NSMO. In both cases, the residual resistivity ρ_o for the ^{18}O samples is larger than for the ^{16}O samples by about 15%. Repeating the van der Pauw measurements at 5 K several times with different contact configurations indicates that the uncertainty of the difference in ρ_o of the two isotope samples is less than 3%. We should mention that the intrinsic resistivity cannot be obtained from ceramic samples where the boundary resistivity is dominant. Thus one cannot use ceramic samples to study the isotope effect on the intrinsic resistivity. Moreover, the van der Pauw technique is particularly good to precisely measure the resistivity difference between the oxygen-isotope exchanged films which have the same thickness. Thus the data shown in Figs. 5 and 6 represent the first precise measurements on the intrinsic resistivity of the isotope substituted samples.

It is known that [33] the residual resistivity $\rho_o \propto m^*/n\tau_o$. Here \hbar/τ_o is the scattering rate which is associated with the random potential produced by randomly distributed trivalent and divalent cations [33], and/or with impurities; m^* is the effective mass of carriers at low temperatures, and n is the mobile carrier concentration. If the chemical potential is far above the mobility edge, $\rho_o \propto (m^*)^2$, that is, $\hbar/\tau_o \propto m^*$. This is what one expects from the simple Born approximation. On the other hand, one can show [34] that $\rho_o \propto m^*$ if the chemical potential is slightly above the mobility edge. Therefore, the large oxygen-isotope effect on ρ_o implies that the effective mass of

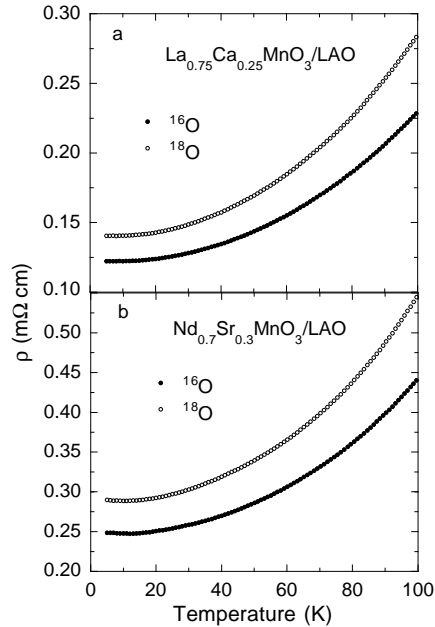


Fig. 6. The low-temperature resistivity of the oxygen-isotope exchanged films of (a) $\text{La}_{0.75}\text{Ca}_{0.25}\text{MnO}_3$; (b) $\text{Nd}_{0.7}\text{Sr}_{0.3}\text{MnO}_3$. After Ref. [31].

the carriers strongly depends on the oxygen mass, as expected for polaronic charge carriers.

If the charge carriers at low temperatures are of small or intermediate-size polarons, the temperature dependence of the resistivity should agree with polaron metallic conduction. This is indeed the case as recently demonstrated by Zhao *et al.* [29]. There are three contributions to the resistivity: the residual resistivity ρ_o , the term $AT^{4.5}$ contributed from 2-magnon scattering [35], and the term $B\omega_s/\sinh^2(\hbar\omega_s/2k_B T)$, which arises from polaron coherent motion involving a relaxation due to a soft optical phonon mode that is strongly coupled to the carriers [29]. Here ω_s is the frequency of a soft optical mode. The temperature dependent part of the resistivity is then given by

$$\rho(T) - \rho_o = AT^{4.5} + B\omega_s/\sinh^2(\hbar\omega_s/2k_B T). \quad (4)$$

It was shown that the parameter B is proportional to m^*/n [29]. This implies that B and ρ_o should have a similar relative change upon the isotope substitution if the chemical potential is near the mobility edge. The coefficient A has an analytical expression in the case of a simple parabolic polaron band (occupied by single-spin holes) [35]. In terms of the hole density per cell n , the

average spin stiffness D , and the effective hopping integral t^* , the coefficient A can be written as [35]

$$A = \left(\frac{3a\hbar}{32\pi e^2} \right) (2 - n/2)^{-2} (6\pi^2 n)^{5/3} \left(2.52 + 0.0017 \frac{D}{a^2 t^*} \right) \left\{ \frac{a^2 k_B}{D(6\pi^2)^{2/3} (0.5^{2/3} - n^{2/3})} \right\}^{9/2}. \quad (5)$$

Here we have used the relations: $ak_F = (6\pi^2 n)^{1/3}$ (where $\hbar k_F$ is the Fermi momentum); $E_F = t^*(6\pi^2)^{2/3} (0.5^{2/3} - n^{2/3})$ (where the Fermi energy E_F is measured from the band center); the effective spin $S^* = 2 - n/2$. The value of t^* can be estimated to be about 40 meV from the measured effective plasma frequency $\hbar\Omega_p^* = 1.1$ eV and $n \sim 0.3$ in $\text{La}_{0.7}\text{Ca}_{0.3}\text{MnO}_3$ [36]. Since D is about 100 meV \AA^2 (see below), one expects that the term $0.0017D/a^2 t^* \ll 2.52$, and thus can be dropped out in Eq. 5.

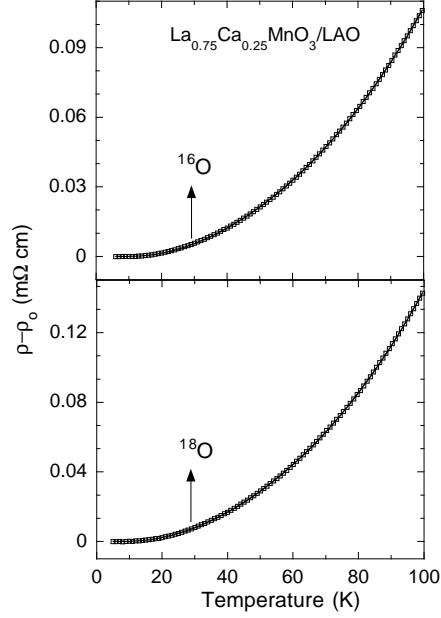


Fig. 7. $\rho(T) - \rho_o$ for the ^{16}O and ^{18}O films of $\text{La}_{0.75}\text{Ca}_{0.25}\text{MnO}_3$. The solid lines are fitted curves by Eq. 4. After Ref. [31].

From Eq. 5, one sees that there are two parameters n and D that determine the magnitude of A . In doped manganites, n should be approximately equal to the doping level x . The average spin stiffness D should be close to the

long-wave spin stiffness $D(0)$ if there is negligible magnon softening near the zone boundary. On the other hand, $D < D(0)$ if there is a magnon softening near the zone boundary as the case of low T_C materials [37]. In any cases, one might expect that the average D should be proportional to T_C so that $D/k_B T_C$ is a universal constant in the manganite system. Since the magnon softening becomes unimportant when the T_C is higher than 350 K [37], then $D \simeq D(0)$ in the compound $\text{La}_{0.7}\text{Sr}_{0.3}\text{MnO}_3$ with the highest $T_C = 378$ K [38]. Thus, the universal value of $D/k_B T_C$ should be close to the value of $D(0)/k_B T_C$ in $\text{La}_{0.7}\text{Sr}_{0.3}\text{MnO}_3$, which was found to $5.8 \pm 0.2 \text{ \AA}^2$ [38].

The $\rho(T) - \rho_o$ data below 100 K are fitted by Eq. 4 for the LCMO ^{16}O and ^{18}O samples, as shown in Fig. 7. It is striking that the fits to the data of both isotope samples are very good. The fitting parameters A , B and $\hbar\omega_s$ are summarized in Table I. Since the fits are excellent, the uncertainties in the fitting parameters are very small (see Table 1). From Table 1, one can see that ρ_o increases by 15(3)%, and B by 17(3)%. This provides additional evidence that the scattering rate \hbar/τ_o is nearly isotope-mass independent, in agreement with the above argument. Thus the observed large oxygen-isotope effects on both ρ_o and B suggest that the effective mass of carriers depends strongly on the oxygen-isotope mass. This is consistent with the presence of small or intermediate-size polarons in the ferromagnetic state of manganites.

In addition, ω_s decreases by about 10(1)% upon replacing ^{16}O with ^{18}O . This may imply that the soft mode might be associated with the motion of the oxygen atoms and has a large anharmonicity. It was shown that the tilt/rotation mode of the oxygen octahedra in cuprates has a strong electron-phonon coupling (quadratic coupling) and a large anharmonicity [39, 40]. The large anharmonicity of the mode can possibly lead to a decrease of ω_s by 12.5% upon replacing ^{16}O with ^{18}O [39]. In a similar perovskite superconductor $\text{Ba}(\text{Pb}_{0.75}\text{Bi}_{0.25})\text{O}_3$, both neutron and tunneling experiments [41] show that a soft mode with $\hbar\omega_s/k_B = 70$ K is related to rotational vibrations of the oxygen octahedra, and has a strong electron-phonon coupling. Moreover, the frequency of the rotational mode in $\text{Ba}(\text{Pb}_{0.75}\text{Bi}_{0.25})\text{O}_3$ is nearly the same as that of the soft mode ($\hbar\omega_s/k_B = 74$ K) in the $\text{La}_{0.75}\text{Ca}_{0.25}\text{MnO}_3$ ^{16}O film. Both the frequency of the soft mode and its isotope dependence can be quantitatively explained if the soft mode in the manganites is also associated with the rotational vibrations of the oxygen octahedra.

Now we turn to the discussion on the magnitude of the parameter A and its isotope dependence. From Eq. 5, one can see that n and/or D should be isotope dependent in order to explain the large isotope effect on the parameter A . As discussed above, the D in Eq. 5 should be proportional to T_C . Then one can obtain D values from the T_C values and the value of $D/k_B T_C = 5.8 \text{ \AA}^2$ (see the above discussion). Substituting the D and A values (see Table 1) into Eq. 5, we find $n = 0.235$ for the $\text{La}_{0.75}\text{Ca}_{0.25}\text{MnO}_3$ ^{16}O film, and $n = 0.240$ for the $\text{La}_{0.75}\text{Ca}_{0.25}\text{MnO}_3$ ^{18}O film. The fact that $n \simeq x$ for both isotope samples is consistent with our previous interpretation of the isotope dependence of

Table 1. The summary of the fitting parameters A , B and $\hbar\omega_s/k_B$ for the ^{16}O and ^{18}O films of $\text{La}_{0.75}\text{Ca}_{0.25}\text{MnO}_3$ (LCMO), and the summary of the T_C and ρ_o values for the LCMO films and the $\text{Nd}_{0.7}\text{Sr}_{0.3}\text{MnO}_3$ films (NSMO). The uncertainty in T_C is ± 0.3 K. The uncertainty in ρ_o is discussed in the text.

Compounds	T_C (K)	ρ_o ($\mu\Omega\text{cm}$)	A ($\text{m}\Omega\text{cm}/\text{K}^{4.5}$)	B ($\mu\Omega\text{cm}/\text{K}$)	$\hbar\omega_s/k_B$ (K)
LCMO(^{16}O)	231.3	122.4	$1.20(2)\times 10^{-11}$	0.370(3)	74.4(2)
LCMO(^{18}O)	217.3	140.5	$1.89(2)\times 10^{-11}$	0.434(3)	66.8(3)
NSMO(^{16}O)	203.9	248.2			
NSMO(^{18}O)	186.4	289.2			

ρ_o being caused only by m^* . The $AT^{4.5}$ term in our resistivity data is in quantitative agreement with the 2-magnon scattering theory [35].

From the oxygen-isotope effects on the residual resistivity and the thermoelectric power at low temperatures, one can deduce the exponent of the oxygen-isotope effect on m^* based on a polaronic Fermi liquid model [34]. The exponent β_O of the oxygen-isotope effect on m^* was estimated [34] to be about -0.7 for $\text{La}_{0.75}\text{Ca}_{0.25}\text{MnO}_3$ and about -1.1 for $\text{Nd}_{0.7}\text{Sr}_{0.3}\text{MnO}_3$. From Eq. 1, one finds that the polaronic mass enhancement factor $m^*/m = \exp(-2\beta) \simeq \exp(-2\beta_O) = 4-9$. This mass enhancement factor is consistent with the existence of intermediate size polarons.

Very recent angle-resolved photoemission spectroscopic data [42] of a layered manganite $\text{La}_{1.2}\text{Sr}_{1.8}\text{Mn}_2\text{O}_7$ ($T_C = 126$ K) suggest the coexistence of bipolaronic carriers (pseudo-gapped state) along the Mn-O binding direction and polaronic charge carriers along the diagonal direction. The polaron mass is enhanced by a factor of 5.6 (Ref. [42]), which is in good agreement that (4-9) obtained from our isotope experiments.

The coexistence of polaronic and bipolaronic carriers in the ferromagnetic state of the layered manganite [42] is also consistent with our earlier results [43, 44] for a 3-dimensional manganite $(\text{La}_{0.5}\text{Nd}_{0.5})_{0.67}\text{Ca}_{0.33}\text{MnO}_3$ with a similar T_C (~ 100 K). The ground state of these low T_C manganites is phase-separated into ferromagnetic metallic regions where mobile polarons reside and charge-ordered insulating regions—where localized bipolarons sit.

2.3 Oxygen-isotope effects on electrical transport above the Curie temperature

The first experimental evidence for small polaronic charge carriers in the paramagnetic state was provided by transport measurements [45]. It was found that the activation energy E_ρ deduced from the conductivity data is one order of magnitude larger than the activation energy E_s obtained from the thermoelectric power data. Such a large difference in the activation energies is the hallmark of the small-polaron hopping conduction. The giant oxygen-isotope

shifts of the ferromagnetic transition temperature T_C give clear evidence for the presence of polaronic charge carriers in this system [22, 23]. Moreover, the fast and local techniques have directly shown that the doped charge carriers are accompanied by local Jahn-Teller distortions [46, 47, 48, 49]. However, all these experiments cannot make a distinction between small polarons and small bipolarons since both are dressed by local lattice distortions. Small bipolarons are normally much heavier than small polarons, and should be localized in the presence of small random potentials. In order to discriminate between polarons and bipolarons and to place constraints on the CMR theories, it is essential to study the oxygen-isotope effects on the intrinsic electrical properties. This is because the activation energies in resistivity and thermoelectric power will depend on the oxygen isotope mass if there coexist localized bipolaronic charge carriers and mobile polaronic carriers.

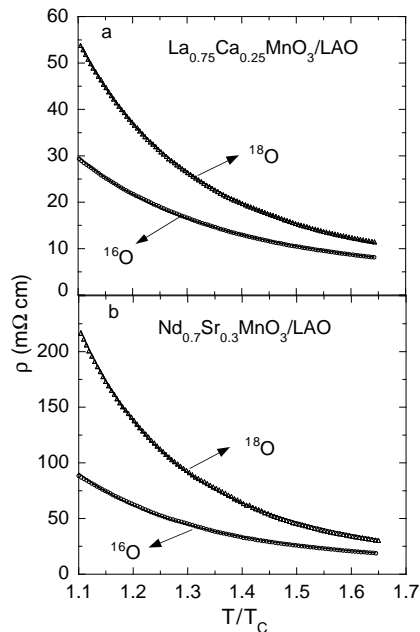


Fig. 8. The resistivity of the oxygen-isotope exchanged films of $\text{La}_{0.75}\text{Ca}_{0.25}\text{MnO}_3$ and $\text{Nd}_{0.7}\text{Sr}_{0.3}\text{MnO}_3$. The maximum temperature of the data points for the ^{16}O film of $\text{La}_{0.75}\text{Ca}_{0.25}\text{MnO}_3$ is 380 K. The solid lines are the fitted curves by Eq. 7. As in Ref. [45], we excluded the data points below $1.1T_C$ for the fitting. After Ref. [50].

Zhao *et al.* [50] have precisely measured resistivity for the oxygen-isotope exchanged high-quality epitaxial thin films of $\text{La}_{0.75}\text{Ca}_{0.25}\text{MnO}_3$ and $\text{Nd}_{0.7}\text{Sr}_{0.3}\text{MnO}_3$, and the thermoelectric power for the oxygen-isotope exchanged ceramic sam-

ples of $\text{La}_{0.75}\text{Ca}_{0.25}\text{MnO}_3$. The data cannot be explained by a simple small-polaron model, but are in quantitative agreement with a model where the formation of localized small bipolarons is essential.

Fig. 8 shows the resistivity of the oxygen-isotope exchanged films of LCMO and NSMO above $1.1T_C$. From the figure, one can see that there is a large difference in the intrinsic resistivity between the two isotope samples. Such a large isotope effect is reversible upon the oxygen isotope back-exchange.

It is known that the resistivity can be generally expressed as $\rho = 1/\sigma = 1/ne\mu$, where n is the mobile carrier concentration and μ is the mobility of the carriers. For adiabatic small-polaron hopping, the mobility is given by [5]

$$\mu = \frac{ed^2}{h} \frac{\hbar\omega_o}{k_B T} \exp(-E_a/k_B T). \quad (6)$$

Here d is the site to site hopping distance, which is equal to $a/\sqrt{2}$ in manganites since the doped holes in this system mainly reside on the oxygen sites [18]; ω_o is the characteristic optical phonon frequency; $E_a = (\eta E_p/2)f(T) - t$; $f(T) = [\tanh(\hbar\omega_o/4k_B T)]/(\hbar\omega_o/4k_B T)$ for $T > \hbar\omega_o/4k_B \simeq 200$ K [51]; E_p is the polaron binding energy; t is the ‘‘bare’’ hopping integral; $\eta \leq 1$ [5, 52]. In the harmonic approximation, E_p is independent of the isotope mass M .

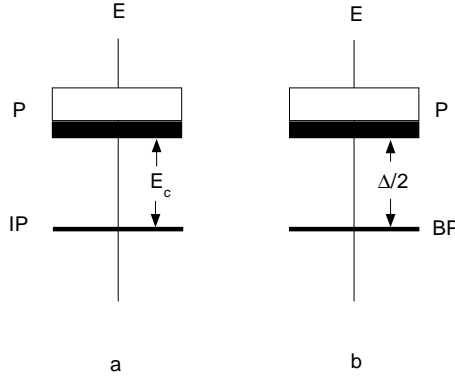


Fig. 9. A schematic diagram of the polaron band, and polaron trapping into impurity (IP) states (a) (Ref. [51]), or into localized bipolaron (BP) states (b) (Ref. [16]). The bipolaron binding energy Δ is isotope-mass dependent [52], while E_c is independent of the isotope-mass M [51]. After Ref. [50].

The mobile polaron density n can be calculated for the two possible cases shown in Fig. 9. If we assume a simple parabolic band, then $n = 2(k_B T/1.05a^2 W_p)^{3/2} \exp(-E_s/k_B T)$ for $T \ll W_p/k_B$ [16, 51]. Here W_p is the polaron bandwidth; $E_s = E_c$ if polarons are trapped into impurity (IP) states [51], while $E_s = \Delta/2$ if polarons are bound into localized bipolaron (BP) states [16]. The bipolaron binding energy $\Delta = 2(1 - \gamma)E_p - V_c - W_p$, where

V_c is the Coulombic repulsion between bound polarons [52]. In fact, the above $n(T)$ expression is the same as that for semiconductors when the chemical potential is pinned to the impurity levels. Using the above $n(T)$ expression and Eq. 6, we finally have

$$\rho = \frac{C}{\sqrt{T}} \exp(E_\rho/k_B T), \quad (7)$$

where $E_\rho = E_a + E_s$, and $C = (ah/e^2\sqrt{k_B})(1.05W_p)^{1.5}/\hbar\omega_o$. The quantity C should strongly depend on the isotope mass M and decrease with increasing M . This is because W_p decreases strongly with increasing M according to $W_p \propto \exp(-\gamma E_p/\hbar\omega_o) = \exp(-g^2)$ [52, 9]. It is worthy of noting that Eq. 7 is valid only if $T \ll W_p/k_B$. For $T \gg W_p/k_B$, the prefactor in Eq. 7 should be proportional to T/ω_o [45].

The thermoelectric power is given by [51]

$$S = E_s/eT + S_o, \quad (8)$$

where S_o is a constant depending on the kinetic energy of the polarons and on the polaron density [51]. One should note that Eq. 8 is valid only if there is one type of carriers (e.g., holes).

One can make a distinction between the two cases shown in Fig. 9. If small polarons are bound to impurity centers, there will be no isotope effect on E_s since E_c is independent of M [51]. On the other hand, if small polarons are bound to localized bipolaron states, both E_ρ and E_s in Eq. 7 and Eq. 8 will depend on M due to the fact that Δ is M dependent. In general, the isotope shift of E_ρ will be larger than the isotope shift of E_s . This is because $E_a = (\eta E_p/2)f(T) - t$, and $f(T) = [\tanh(\hbar\omega_o/4k_B T)]/(\hbar\omega_o/4k_B T)$, which may depend on M if the temperature is not so high compared with $\hbar\omega_o/k_B$.

The data are now fitted by Eq. 7 (see solid lines in Fig. 8). It is apparent that the fits are quite good for both isotope samples. The fitting parameters are summarized in Table 2. From Table 2, one can see that, upon replacing ^{16}O with ^{18}O , the parameter C for LCMO/NSMO decreases by 35(5)/40(7)%, while E_ρ increases by 13.2(3)/14.2(8) meV. The huge oxygen-isotope effect on the parameter C is consistent with Eq. 7.

One can obtain the isotope shift of E_s by measuring the thermoelectric power for two isotope samples according to Eq. 8. In Fig. 10, the thermoelectric power S as a function of $1/T$ is plotted for the ^{16}O and ^{18}O samples of $\text{La}_{0.75}\text{Ca}_{0.25}\text{MnO}_3$. Both T_C 's and the isotope shift of the ceramic samples [25] are the same as those in the corresponding thin films. Since the grain-boundary effect on S is negligible, the thermoelectric power obtained in ceramic samples should be intrinsic. From the slopes of the straight lines in Fig. 10, one finds $E_s = 13.2 \pm 0.3$ meV for the ^{16}O sample and 18.7 ± 0.3 meV for the ^{18}O . The isotope shift is $\delta E_s = 5.5 \pm 0.6$ meV, which is about half the isotope shift of E_ρ . The observed oxygen-isotope effects on both E_ρ and E_s do not support a simple small-polaron model [51], but provide evidence that small polarons are bound into localized bipolaron states.

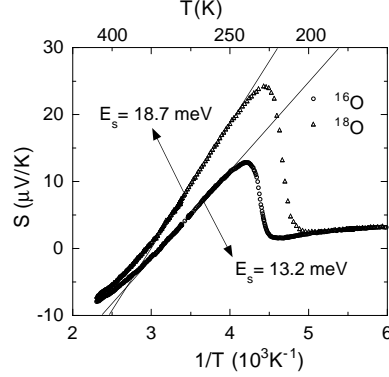


Fig. 10. The thermoelectric power $S(T)$ of the oxygen-isotope exchanged ceramic samples of $\text{La}_{0.75}\text{Ca}_{0.25}\text{MnO}_3$. After Ref. [50].

One can use the values of the parameter C to calculate the polaron bandwidth W_p according to the relation: $C = (ah/e^2\sqrt{k_B})(1.05W_p)^{1.5}/\hbar\omega_o$. The calculated W_p values are listed in Table 2. In the calculation, $\hbar\omega_o = 74$ meV is used for the ^{16}O samples [52], and $\hbar\omega_o$ for the ^{18}O samples is 5.7% lower than for the ^{16}O samples. From the W_p values (see Table 2), one can see that the data satisfy $T < W_p/k_B$, which justifies the use of Eq. 7.

Furthermore, one can quantitatively explain the isotope dependence of E_s if small polarons form localized bipolarons. In this scenario [52], $\delta\Delta = -\delta W_p$. From Table 2, $\delta W_p = -11.2 \pm 1.6$ meV for $\text{La}_{0.75}\text{Ca}_{0.25}\text{MnO}_3$. So $\delta E_s = \delta\Delta/2 = 5.6 \pm 0.8$ meV for $\text{La}_{0.75}\text{Ca}_{0.25}\text{MnO}_3$, in quantitative agreement with the value (5.5 ± 0.6 meV) deduced from the thermoelectric power data.

Table 2. Summary of the fitting and measured parameters for the ^{16}O and ^{18}O films of $\text{La}_{0.75}\text{Ca}_{0.25}\text{MnO}_3$ (LCMO) and $\text{Nd}_{0.7}\text{Sr}_{0.3}\text{MnO}_3$ (NSMO). The errors of the parameters come from the fitting and from the van der Pauw measurement. The absolute uncertainty of the thickness of the films was not included in the error calculations since it only influences the absolute values of the resistivity.

Compounds	LCMO(^{16}O)	LCMO(^{18}O)	NSMO(^{16}O)	NSMO(^{18}O)
T_C (K)	231.5(3)	216.5(3)	204(1)	186(1)
C ($\text{m}\Omega\text{cmK}^{0.5}$)	17.3(5)	12.9(3)	23.2(8)	16.2(7)
E_ρ (meV)	72.8(2)	86.0(1)	78.8(4)	92.9(4)
E_s (meV)	13.2(3)	18.7(3)		
W_p (meV)	49.0(9)	38.8(7)	60(2)	45(2)

Therefore, the oxygen isotope effects on the intrinsic electrical transport in the paramagnetic state of doped manganites can be quantitatively explained by a scenario [16] where the small polarons form localized bound pairs (bipo-

larons) in the paramagnetic state. The coexistence of small polarons and bipolarons in the paramagnetic state may lead to a dynamic phase separation into the insulating antiferromagnetically coupled region where the bipolarons reside, and into the ferromagnetically coupled region where the polarons sit. This simple picture can naturally explain the observation of the ferromagnetic clusters (intrinsic electronic inhomogeneity) in the paramagnetic state [53].

3 Polarons in cuprates

Developing the microscopic theory for high- T_c superconductivity is one of the most challenging problems in condensed matter physics. Eighteen years after the discovery of the high- T_c cuprate superconductors by Bednorz and Müller [1], there have been no microscopic theories that can describe the physics of high- T_c superconductors completely and unambiguously. Due to the high T_c values and the observation of a small oxygen-isotope effect in a 90 K cuprate superconductor $\text{YBa}_2\text{Cu}_3\text{O}_{7-y}$ (YBCO) [54, 55], many theorists believe that the electron-phonon interaction is not important in bringing about high- T_c superconductivity. Most physicists have thus turned their minds towards alternative pairing interactions of purely electronic origin.

On the other hand, there is overwhelming evidence that electron-phonon coupling is very strong in cuprates [56, 57, 58, 59, 60, 61, 62, 63, 64, 65, 66, 67, 68, 69, 70, 71]. In particular, the studies of various unconventional oxygen-isotope effects Zhao and his coworkers have initiated since 1992 clearly indicate that the electron-phonon interactions are so strong that polarons/bipolarons are formed in doped cuprates and manganites [56, 57, 58, 59, 60, 62, 63, 64, 65, 66, 67, 69, 22], in agreement with a theory of high-temperature superconductivity [6]. However, such clear experimental evidence for strong electron-phonon interactions from the unconventional isotope effects has been generally ignored. In the 2001 Nature paper [68], Lanzara *et al.* appear to provide evidence for a strong coupling between doped holes and the 70 meV half-breathing phonon mode from angle-resolved photoemission spectroscopy (ARPES). They further show that this 70 meV phonon mode can lead to d-wave pairing symmetry and is mainly responsible for high-temperature superconductivity [72]. Recently, Devereaux *et al.* [73] have proposed that the 40 meV B_{1g} phonon mode rather than 70 meV half-breathing phonon mode is responsible for d-wave high-temperature superconductivity. This pairing mechanism contradicts the very recent ARPES data from their own group, which show that multiple phonon modes at 27 meV, 45 meV, 61 meV, and 75 meV are strongly coupled to doped holes in deeply underdoped $\text{La}_{2-x}\text{Sr}_x\text{CuO}_4$ [70]. The strong coupling to the multiple phonon modes is not in favor of d-wave gap symmetry but may support a general s-wave gap symmetry [74, 75].

3.1 Oxygen-isotope effect on T_N in La_2CuO_4

The antiferromagnetic order (AF) observed in the parent insulating compounds like La_2CuO_4 signals a strong electron-electron Coulomb correlation. On the other hand, if there is a very strong electron-phonon coupling such that the Migdal adiabatic approximation breaks down, one might expect that the antiferromagnetic exchange energy should depend on the isotope mass. Following this simple argument, Zhao and his co-workers initiated studies of the oxygen isotope effect on the AF ordering temperature in several parent compounds in 1992. A noticeable oxygen-isotope shift of T_N was consistently observed in La_2CuO_4 [56].

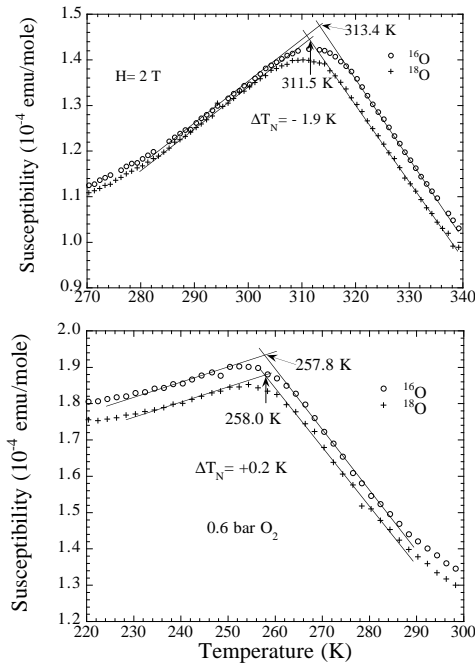


Fig. 11. The temperature dependence of the susceptibility for the ^{16}O and ^{18}O samples of undoped La_2CuO_4 (upper panel), and of the oxygen-doped $\text{La}_2\text{CuO}_{4+y}$ (lower panel). After [56].

Fig. 11 shows the temperature dependence of the susceptibility for the ^{16}O and ^{18}O samples of undoped La_2CuO_4 (upper panel), and of oxygen doped $\text{La}_2\text{CuO}_{4+y}$ (lower panel). One can see that the AF ordering temperature T_N for the ^{18}O sample is lower than the ^{16}O sample by about 1.9 K in the case

of the undoped samples. For the oxygen-doped samples, there is a negligible isotope effect.

It is known that the antiferromagnetic properties of $\text{La}_2\text{CuO}_{4+y}$ can be well understood within mean-field theory which leads to a T_N formula [76]:

$$k_B T_N = J' [\xi(T_N)/a]^2, \quad (9)$$

where J' is the interlayer coupling energy, $\xi(T_N)$ is the in-plane AF correlation length at T_N with $\xi(T_N) \propto \exp(J/T_N)$ for $y = 0$ (J is the in-plane exchange energy). When T_N is reduced to about 250 K by oxygen doping, a mesoscopic phase separation has taken place so that $\xi(T_N) = L$ (Ref. [77]), where L is the size of the antiferromagnetically correlated clusters, and depends only on the extra oxygen content y . In this case, we have $T_N = J'(L/a)^2$. Since L is independent of the isotope mass, a negligible isotope shift of T_N in the oxygen-doped $\text{La}_2\text{CuO}_{4+y}$ suggests that J' is independent of the isotope mass. Then we easily find for undoped compounds

$$\Delta T_N/T_N = (\Delta J/J) \frac{B}{1+B}, \quad (10)$$

where $B = 2J/T_N \simeq 10$. From the measured isotope shift of T_N for the undoped samples, we obtain $\Delta J/J \simeq -0.6\%$.

Recently, Eremin *et al.* [78] have considered strong electron-phonon coupling within a three-band Hubbard model. They showed that the antiferromagnetic exchange energy J depends on the polaron binding energy E_p^O due to oxygen vibrations, on the polaron binding energy E_p^{Cu} due to copper vibrations, and on their respective vibration frequencies ω_O and ω_{Cu} . At low temperatures, J is given by [78]

$$J = J_o \left(1 + \frac{3E_p^O \hbar \omega_O}{\Delta_{pd}^2} + \frac{3E_p^{Cu} \hbar \omega_{Cu}}{\Delta_{pd}^2} \right). \quad (11)$$

Here Δ_{pd} is the charge-transfer gap, which is measured to be about 1.5 eV in undoped cuprates. The oxygen-isotope effect on J can be readily deduced from Eq. 11:

$$\frac{\Delta J}{J} = \left(\frac{3E_p^O \hbar \omega_O}{\Delta_{pd}^2} \right) \left(\frac{\Delta \omega_O}{\omega_O} \right). \quad (12)$$

Substituting the unbiased parameters $\hbar \omega_O = 0.075$ eV, $\Delta J/J \simeq -0.6\%$, $\Delta_{pd} = 1.5$ eV, and $\Delta \omega_O/\omega_O = 6.0\%$ into Eq. 12, we find that $E_p^O = 1.0$ eV. The total polaron binding energy should be larger than 1.0 eV since E_p^{Cu} is not zero.

The polaron binding energy can be also estimated from optical data where the energy of the mid-infrared peak in the optical conductivity is equal to $2\gamma E_p$ (Ref.[52]), where γ is between 0.2-0.3 (Ref.[52]). The peak position ($2\gamma E_p$) was found to be about 0.6 eV for $\text{La}_{1.97}\text{Sr}_{0.03}\text{CuO}_4$ (Ref. [79]), implying that E_p

= 1.0-1.5 eV. This is in quantitative agreement with the value estimated from the isotope effect. These results thus consistently suggest that the polaron binding energy of undoped La_2CuO_4 is over 1 eV. Doping will reduce the value of E_p due to screening. For the optimal doping ($x = 0.15$), the optical data suggest that $2\gamma E_p = 0.12$ eV, which is a factor of 5 smaller than that for $x = 0.03$.

Very recently, angle-resolved photoemission spectroscopy (ARPES) data of undoped La_2CuO_4 have been explained in terms of polaronic coupling between phonons and charge carriers [80]. From the width of the phonon side band in the ARPES spectra, the authors find the polaron binding energy to be about 1.9 eV, in good agreement with their theoretical calculation based on a shell model [80]. On the other hand, the observed binding energy of the side band should be consistent with a polaron binding energy of about 1.0 eV (Ref. [80]). This should be the lower limit because the binding energy of the side band decreases rapidly with doping and because the sample may be lightly doped [80]. Therefore, the ARPES data suggest that $1.0 \text{ eV} < E_p < 1.9 \text{ eV}$, which is in quantitative agreement with the value deduced from our earlier isotope experiments.

3.2 Oxygen-isotope effect on the in-plane supercarrier mass

One of the most remarkable oxygen-isotope effects we have observed is the oxygen-isotope effect on the penetration depth [57, 58, 59, 60, 64, 65, 66, 67, 69]. Zhao *et al.* made the first observation of this effect in optimally doped $\text{YBa}_2\text{Cu}_3\text{O}_{6.93}$ in 1994 [57]. By precisely measuring the diamagnetic signals for the ^{16}O and ^{18}O samples, one were able to deduce the oxygen-isotope effects on the penetration depth $\lambda(0)$ and on the supercarrier density n_s . It turns out that $\Delta n_s \simeq 0$, and $\Delta\lambda(0)/\lambda(0) = 3.2 \%$ (Ref. [57]). These isotope effects thus suggest that the effective supercarrier mass depends on the oxygen-isotope mass.

In fact, for highly anisotropic materials, the observed isotope effect on the angle-averaged $\lambda(0)$ is the same as the isotope effect on the in-plane penetration depth $\lambda_{ab}(0)$. From the magnetic data for $\text{YBa}_2\text{Cu}_3\text{O}_{6.93}$, $\text{La}_{1.85}\text{Sr}_{0.15}\text{CuO}_4$, and $\text{Bi}_{1.6}\text{Pb}_{0.4}\text{Sr}_2\text{Ca}_2\text{Cu}_3\text{O}_{10+y}$, one finds that $\Delta\lambda_{ab}(0)/\lambda_{ab}(0) = 3.2 \pm 0.7\%$ for the three optimally doped cuprates [67]. Several independent experiments have consistently shown that the carrier densities of the two isotope samples are the same within 0.0004 per unit cell [59, 60, 65]. Therefore, the observed oxygen-isotope effect on the in-plane penetration depth is caused only by the isotope dependence of the in-plane supercarrier mass. Recently, direct measurements of the in-plane penetration depth by low energy muon-spin-relaxation (LE μ SR) technique [69] have confirmed the earlier isotope-effect results. It is found that [69] $\Delta\lambda_{ab}(0)/\lambda_{ab}(0) = 2.8 \pm 1.0\%$. It is remarkable that the isotope effect obtained from the most advanced and expensive technology (LE μ SR) is the same as that deduced from simple magnetic measurements.

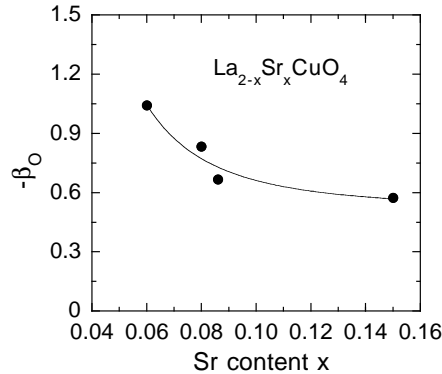


Fig. 12. The doping dependence of the exponent (β_O) of the oxygen-isotope effect on the in-plane supercarrier mass in $\text{La}_{2-x}\text{Sr}_x\text{CuO}_4$. The exponent is defined as $\beta_O = -d \ln m_{ab}^{**} / d \ln M_O$. The data are from Ref. [64, 66, 67].

Fig. 12 shows the doping dependence of the exponent (β_O) of the oxygen-isotope effect on the in-plane supercarrier mass in $\text{La}_{2-x}\text{Sr}_x\text{CuO}_4$. Here the exponent is defined as $\beta_O = -d \ln m_{ab}^{**} / d \ln M_O$. It is apparent that the exponent increases with decreasing doping, in agreement with the fact that doping reduces electron-phonon coupling due to screening. The large oxygen-isotope effect on the in-plane supercarrier mass cannot be explained within the conventional phonon-mediated pairing mechanism where the effective mass of supercarriers is independent of the isotope mass [81]. In particular, the substantial oxygen-isotope effect on m_{ab}^{**} in optimally doped cuprates indicates that the polaronic effect is not vanished in the optimal doping regime where the BCS-like superconducting transition occurs. This suggests that polaronic carriers may be bounded into the Cooper pairs in optimally doped and over-doped cuprates.

3.3 Strong electron-phonon coupling features along the diagonal direction

In conventional superconductors, strong electron-phonon coupling features can be identified from single-particle tunneling spectra. For high- T_c cuprates, high-quality tunneling spectra are difficult to obtain because of a short coherence length. Moreover, due to a strong gap anisotropy, the energies of the strong coupling features will depend on the tunneling directions. Only if one can make a directional tunneling, one may be able to identify the electron-phonon coupling features from the tunneling spectrum. On the other hand, the observation of the electron self-energy renormalization effect in the form of a “kink” in the band dispersion may reveal coupling of electrons with phonon modes. The “kink” feature at an energy of about 65 meV has been seen in the band dispersion of various cuprate superconductors along the diagonal

(“nodal”) direction [68]. From the measured dispersion, one can extract the real part of electron self-energy that contains information about coupling of electrons with collective boson modes. The energy of a broad peak in the electron self-energy should correspond to the averaged energy of all the bosonic modes that couple to electrons if the superconducting gap is zero along the diagonal direction. The fine coupling structures can be only revealed in the high-resolution ARPES data. Very recently, such fine coupling structures have been clearly seen in the raw data of electron self-energy of deeply underdoped $\text{La}_{2-x}\text{Sr}_x\text{CuO}_4$ along the diagonal direction [70]. Using the maximum entropy method (MEM) procedure, they are able to extract the electron-phonon spectral density $\alpha^2F(\omega)$ that contains coupling features at 27 meV, 45 meV, 61 meV and 75 meV. These ARPES data and exclusive data analysis [70] clearly indicate that the phonons rather than the magnetic collective mode are responsible for the electron self-energy effect.

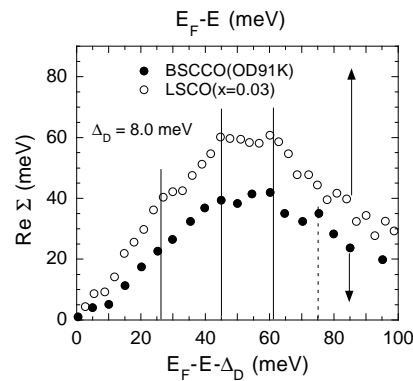


Fig. 13. The real part of electron self-energy along the diagonal direction for a slightly overdoped BSCCO with $T_c = 91$ K (OD91K) [82] and for $\text{La}_{2-x}\text{Sr}_x\text{CuO}_4$ with $x = 0.03$ (Re. [70]). The energy scale for BSCCO is shifted down by $\Delta_D = 8.0$ meV. The solid vertical lines (27 meV, 45 meV, 61 meV) mark the energies of the pronounced phonon peaks in the electron-phonon spectral density $\alpha^2F(\omega)$ that is determined from the MEM procedure [70]. The dashed vertical line indicates the energy of a pronounced phonon peak (75 meV) in the superconducting LSCO with $x = 0.07$.

In fact, the fine coupling structures also appear in the earlier high-resolution ARPES data of a slightly overdoped BSCCO with $T_c = 91$ K (OD91K) [82]. Fig. 13 shows the real part of electron self-energy along the diagonal direction for the OD91K sample. In the same figure, plotted is the real part of electron self-energy along the diagonal direction for $\text{La}_{2-x}\text{Sr}_x\text{CuO}_4$ (LSCO) with $x = 0.03$. One can clearly see the fine structures in the raw data of both LSCO and BSCCO. The solid vertical lines mark the energies of the pronounced phonon peaks (27 meV, 45 meV, 61 meV) in the electron-phonon

spectral density $\alpha^2 F(\omega)$ that is determined from the MEM procedure [70]. The dashed vertical line indicates the energy of a pronounced phonon peak (75 meV) in the superconducting LSCO with $x = 0.07$. In order for the fine structures in the self-energy of BSCCO to be aligned with those for LSCO, the energy scale for BSCCO has to be shifted down by $\Delta_D = 8.0$ meV. This suggests that the superconducting gap along the diagonal direction is not zero. This is consistent with an extended s-wave gap symmetry that has a finite gap of about 10 meV along the diagonal direction [74]. The magnitude of Δ_D surely depends on impurities and disorder, so it may vary from samples to samples.

It is interesting to note that the coupling feature at 75 meV is invisible in the deeply underdoped LSCO ($x = 0.03$), but becomes pronounced in the superconducting LSCO ($x = 0.07$) and in BSCCO (OD91K). This is consistent with the neutron experiments that clearly demonstrate that the coupling to the 75 meV half-breathing mode increases with increasing doping [61]. Nevertheless, the electron-phonon coupling constant for this mode is still small (< 0.2) due to a high phonon energy. This implies that this mode alone cannot cause high-temperature superconductivity, in contrast with the claim by Lanzara *et al.* [68]. In fact, the low energy phonon modes below 30 meV along the diagonal direction in LSCO ($x = 0.03$) contribute a large electron-phonon coupling constant (about 0.8).

3.4 Strong electron-phonon coupling features along the antinodal direction

The electron self-energy effect along the antinodal direction has been studied for several BSCCO crystals (OD91K, OD71K, and OD58K) [83]. The kink feature in the band dispersion in the antinodal direction is much stronger than that along the diagonal direction. This indicates a much stronger electron-boson coupling. One of the puzzling issues is that the averaged energy of the boson modes shifts to a much lower energy (about 20 meV) [83]. Fig. 14 shows the boson energy as a function of the antinodal gap Δ_M for several overdoped BSCCO. The boson energy is calculated according to $E_{boson} = E_{kink} - \Delta_M$, where E_{kink} is the kink energy in the band dispersion. Since the antinodal gap Δ_M was found to be very close to the peak energy in the energy distribution curve (EDC) [84], one can simply take Δ_M being equal to the EDC peak energy. One can see that the boson energy is about 20 meV for heavily overdoped BSCCO and about 16 meV for nearly optimally doped BSCCO. The strong coupling feature at about 20 meV agrees with the electron-boson spectral density $\alpha^2 F(\omega)$ deduced from a break-junction spectrum, as shown in Fig. 15. The spectral density clearly shows strong coupling features at about 20 meV, 35 meV, 60 meV, and 72 meV. In particular, the coupling to phonon modes near 20 meV is strongly enhanced (the coupling constant for the 20 meV phonon peak is about 2.6). This unusual enhancement is possible if the extended van Hove singularity is about 20 meV below the Fermi level and

the electron-phonon matrix element for the 20 meV phonon modes has a maximum around $\mathbf{q} = 0$, where \mathbf{q} is the phonon wavevector. The large density of states at the van Hove singularity (20 meV below the Fermi level) and strong Fermi surface nesting along the antinodal direction greatly enhance the phase space available for 20 meV small- \mathbf{q} phonons to scatter quasiparticles from the states near the antinodal regime to the extended saddle points. The first principle calculation indeed shows that unusual long-range Madelung-like interactions lead to very large matrix elements especially for zone center modes that are related to vibrations of cations (e.g., La, Sr, Ba, Ca) [86]. The phonon energies for the vibrations of the cations are between 15 meV to 25 meV.

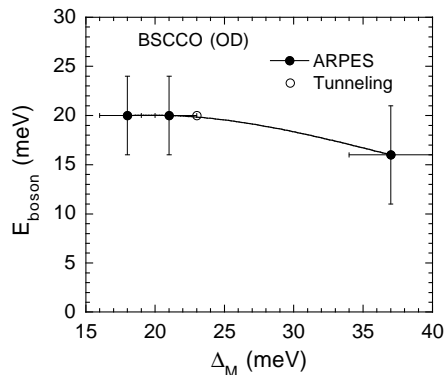


Fig. 14. The boson energy as a function of the antinodal gap Δ_M for several overdoped BSCCO. The boson energy extracted from ARPES (Ref. [83]) is calculated according to $E_{boson} = E_{kink} - \Delta_M$, where E_{kink} is the kink energy in the band dispersion. One data point (open circle) is from the tunneling data (see Fig. 15).

Further, a strong coupling feature in optical data, which was previously explained as due to a strong coupling between electrons and the magnetic resonance mode [87, 88], is actually consistent with a strong electron-phonon coupling at a phonon energy of about 20 meV. It is known that the electron-phonon spectral density $\alpha^2 F(\omega)$ can be obtained through inversion of optical data. Marsiglio *et al.* [89] introduced a dimensionless function $W(\omega)$ which is defined as the second derivative of the normal state optical scattering rate $\tau^{-1}(\omega) = (\Omega_p^2/4\pi)\Re\sigma^{-1}(\omega)$ multiplied by frequency ω . Here Ω_p is the bare plasma frequency and $\sigma(\omega)$ the normal state optical conductivity. Specifically,

$$W(\omega) = \frac{1}{2\pi} \frac{d^2}{d\omega^2} \frac{\omega}{\tau(\omega)} \quad (13)$$

which follows directly from experiment. Marsiglio *et al.* [89] made the very important observation that within the phonon range $W(\omega) \simeq \alpha^2 F(\omega)$.

In the superconducting state, a phonon mode that is strongly coupled to electrons will appear at an energy of $2\Delta(\mathbf{k}) + \omega_{ph}$ (where ω_{ph} is the phonon

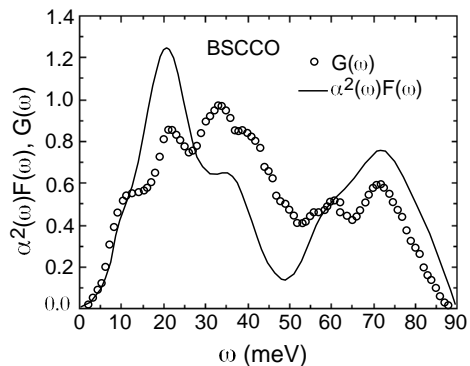


Fig. 15. The electron-phonon spectral density $\alpha^2 F(\omega)$ for a slightly overdoped $\text{Bi}_2\text{Sr}_2\text{CaCu}_2\text{O}_{8+y}$ (BSCCO) crystal, which was deduced from an SIS break-junction spectrum [85].

energy), that is, the energies of the phonon structures shift up by the pair-breaking energy $2\Delta(\mathbf{k})$ [90]. Because the 20 meV phonon modes are much more strongly coupled to the states near the antinodal regime and because there is a large quasiparticle density of states at the maximum gap edge, there must be a maximum at $2\Delta_M + \omega_{ph}$ in $W(\omega)$. For slightly overdoped BSCCO with $T_c = 90$ K, $\Delta_M = 26.0(5)$ meV (Ref.[91, 74]), so we should expect a maximum in $W(\omega)$ to be at about 72 meV. This is in quantitative agreement with the result shown in Fig. 16.

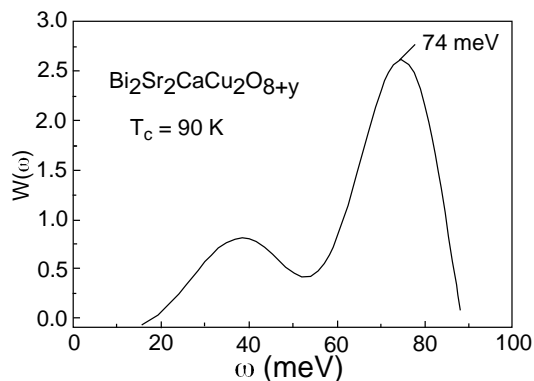


Fig. 16. The optically determined electron-boson spectral density $W(\omega)$ for a slightly overdoped BSCCO crystal with $T_c = 90$ K. After [88].

Recently, Devereaux *et al.* have calculated the electron-phonon interactions for the oxygen buckling mode (B_{1g}) and the in-plane half-breathing mode [73].

They find that the 40 meV B_{1g} mode couples strongly to electronic states near the antinodal regime. They use an electron-phonon matrix element that is suitable only for $\text{YBa}_2\text{Cu}_3\text{O}_{7-y}$ where a large buckling distortion occurs. For other cuprates, the CuO_2 plane is flat and the buckling effect is negligible. Raman data have indeed shown that the coupling constant of the B_{1g} mode in BSCCO is more than one order of magnitude smaller than that in YBCO (Ref. [92]). Even for YBCO, the coupling constant of this mode was deduced to be about 0.05 from the Raman data [92], in agreement with the earlier first principle calculation [93]. Moreover, if this 40 meV phonon were strongly coupled to the electronic states near the antinodal regime, one would expect a maximum in $W(\omega)$ to occur at about 92 meV in slightly overdoped BSCCO with $T_c = 90$ K. This is in total disagreement with experiment (see Fig. 16).

Previously, the energy of the maximum in $W(\omega)$ was claimed to be in quantitative agreement with the theoretical prediction based on the strong coupling between electrons and the magnetic resonance mode [87, 88]. Later on, more rigorous theoretical approach [94] shows that the maximum in $W(\omega)$ should occur at about $2\Delta_M + E_r$ rather than at $\Delta_M + E_r$, where E_r is the magnetic resonance energy. For BSCCO with $T_c = 90$ K, $E_r = 43$ meV, so we should expect a maximum in $W(\omega)$ to occur at about 95 meV, in disagreement with experiment (see Fig. 16)

The strong electron-phonon coupling feature at about 20 meV is also consistent with the energy distribution curves obtained from ARPES. For a conventional strong-coupling superconductor (e.g., Pb), a dip feature in the single-particle density of states can be clearly seen in the superconducting state. The dip feature appears near $\Delta + \omega_c$, where ω_c is the phonon cut-off energy [81]. From Fig. 15, one can see that the cut-off energy for the 20 meV phonon peak is about 40 meV, i.e., $\omega_c \simeq 40$ meV. Since the intensity of EDC is proportional to the single-particle spectral weight, the dip feature should appear in EDC at $\Delta_M + \omega_c$. Because Δ_M is close to the EDC peak energy along the antinodal direction, the separation energy between the peak and dip in the EDC should be close to $\omega_c \simeq 40$ meV, in agreement with experiment [66].

4 Conclusion

The various unconventional oxygen-isotope effects observed in both manganites and cuprates clearly demonstrate the existence of polaronic/bipolaronic charge carriers due to strong electron-phonon coupling. The very recent angle-resolved photoemission spectra for both manganites and cuprates [42, 80] have confirmed our earlier conclusions from the unconventional isotope effects. The formation of polarons/bipolarons in both manganites and cuprates plays an important role in the basic physics of these materials and is essential for the occurrence of colossal magnetoresistance and high-temperature superconductivity. We further show that strong electron-phonon coupling with the 20

meV phonon modes in cuprates are also important to the pairing mechanism of high-temperature superconductivity.

Acknowledgment: This research is partly supported by a Cottrell Science Award from Research Corporation.

References

1. J. G. Bednorz and K. A. Müller, Z. Phys. B **64**, 189 (1986). **332**, 814 (1988).
2. R. von Helmolt, J. Wecker, B. Holzapfel, L. Schultz, and K. Samwer, Phys. Rev. Lett. **71**, 2331 (1993); S. Jin, T. H. Tiefel, M. McCormack, R. A. Fastnacht, R. Ramesh, and L. H. Chen, Science **264**, 413 (1994).
3. L. D. Landau, Phys. Z. Sowjetunion **3**, 664 (1933).
4. T. Holstein, Ann. Phys. (N. Y.), **8**, 325 (1959).
5. D. Emin and T. Holstein, Ann. Phys. (N. Y.), **53**, 439 (1969).
6. A. S. Alexandrov and N. F. Mott, *Polarons and Bipolarons*, 67-106 (World Scientific, Singapore, 1995).
7. Devreese, J. T. in Encyclopedia of Applied Physics, vol. 14, p. 383, VCH Publishers (1996); J. Tempere and J. T. Devreese, Phys. Rev. B **64**, 104504 (2001); J. T. Devreese (in the present volume).
8. A. S. Alexandrov, Phys. Rev. B **61**, 12315 (2000).
9. A. S. Alexandrov and P. E. Kornilovitch, Phys. Rev. Lett. **82**, 807 (1999).
10. E. O. Wollan, and W. C. Koeler, Phys. Rev. **100**, 545 (1955).
11. G. H. Jonker, and J. H. van Santen, Physica **16**, 337 (1950).
12. C. Zener, Phys. Rev. **82**, 403 (1951).
13. P. W. Anderson, and H. Hasegawa, Phys. Rev. **100**, 675 (1955).
14. A. J. Millis, P. B. Littlewood, and B. I. Shraiman, Phys. Rev. Lett. **74**, 5144 (1995).
15. A. J. Millis, B. I. Shraiman, and R. Mueller, Phys. Rev. Lett. **77**, 175 (1996); H. Röder, J. Zang, and A. R. Bishop, Phys. Rev. Lett. **76**, 1356 (1996).
16. A. S. Alexandrov and A. M. Bratkovsky, Phys. Rev. Lett. **82**, 141 (1999); A. S. Alexandrov and A. M. Bratkovsky, J. Phys.:Condens. Matter, **11**, 1989 (1999).
17. A. J. Millis, Nature **392**, 147 (1998).
18. H. L. Ju *et al.*, Phys. Rev. Lett. **79**, 3230 (1997).
19. T. Saitoh *et al.*, Phys. Rev. B **51**, 13942 (1995).
20. G. M. Zhao, Phys. Rev. B **62**, 11 639 (2001).
21. G.-M. Zhao and D. E. Morris, 1995 (unpublished).
22. G.-M. Zhao, K. Conder, H. Keller, and K. A. Müller, Nature **381**, 676 (1996).
23. G. M. Zhao, M. B. Hunt and H. Keller, Phys. Rev. Lett. **78**, 955 (1997).
24. J.-S. Zhou and J. B. Goodenough, Phys. Rev. Lett. **80**, 2665 (1998).
25. G. M. Zhao *et al.*, Phys. Rev. B **60**, 11 914 (1999).
26. A. Urushibara *et al.*, Phys. Rev. B **51**, 14103 (1995).
27. M. Jaime *et al.*, Phys. Rev. B **58**, R5901 (1998).
28. A. Machida, Y. Moritomo, and A. Nakamura, Phys. Rev. B **58**, R4281 (1998).
29. G. M. Zhao *et al.*, Phys. Rev. Lett. **84**, 6086 (2000).
30. A. Moreo, S. Yunoki, and E. Dagotto, Science **283**, 2034 (1994).

31. G. M. Zhao *et al.*, Phys. Rev. B **63**, 060402R (2000).
32. W. Prellier *et al.*, Appl. Phys. Lett. **75**, 1446 (1999).
33. W. E. Pickett and D. J. Singh, Phys. Rev. B **55**, R8642 (1997); D. A. Papaconstantopoulos and W. E. Pickett, Phys. Rev. B **57**, 12751 (1998).
34. A. S. Alexandrov, G. M. Zhao, H. Keller, B. Lorenz, Y. S. Wang, and C. W. Chu, Phys. Rev. B **64**, R140404 (2001).
35. K. Kubo and N. A. Ohata, J. Phys. Soc. Jpn. **33**, 21 (1972).
36. J. R. Simpson *et al.*, Phys. Rev. B **60**, R16 263 (1999).
37. H. Y. Hwang *et al.*, Phys. Rev. Lett. **80**, 1316 (1998).
38. M. C. Martin *et al.*, Phys. Rev. B **53**, 14 285 (1996).
39. V. H. Crespi and M. L. Cohen, Phys. Rev. B **48**, 398 (1993).
40. W. E. Pickett, R. E. Cohen, and H. Krakauer, Phys. Rev. Lett. **67**, 228 (1991).
41. W. Reichardt, B. Batlogg, and J. P. Remeika, Physica B **135**, 501 (1985).
42. N. Mannella *et al.*, Nature **438**, 474 (2005).
43. G. M. Zhao *et al.*, Solid State Commun. **104**, 57 (1997)
44. M. R. Ibarra, G. M. Zhao, J. M. De Teresa, B. Garcia-Landa, Z. Arnold, C. Marquina, P. A. Algarabel, and H. Keller, Phys. Rev. B **57**, 7446 (1998).
45. M. Jaime, M. B. Salamon, M. Rubinstein, R. E. Treece, J. S. Horwitz, and D. B. Chrisey, Phys. Rev. B **54**, 11914 (1996).
46. S. J. L. Billinge, R. G. DiFrancesco, G. H. Kwei, J. J. Neumeier, and J. D. Thompson, Phys. Rev. Lett. **77**, 715 (1996).
47. C. H. Booth, F. Bridges, G. H. Kwei, J. M. Lawrence, A. L. Cornelius, and J. J. Neumeier, Phys. Rev. Lett. **80**, 853 (1998).
48. D. Louca, T. Egami, E. L. Brosha, H. Röder, and A. R. Bishop, Phys. Rev. B **56**, R8475 (1997).
49. A. Lanzara, N. L. Saini, M. Brunelli, F. Natali, A. Bianconi, P. G. Radelli, and S. W. Cheong, Phys. Rev. Lett. **81**, 878 (1998).
50. G. M. Zhao *et al.*, Phys. Rev. B **63**, 11949R (2000).
51. I. G. Austin and N. F. Mott, Adv. Phys. **18**, 41 (1969).
52. A. S. Alexandrov and A. M. Bratkovsky, J. Phys.: Condens. Matter, **11**, L531 (1999).
53. J. M. De Teresa, M. R. Ibarra, P. A. Algarabel, C. Ritter, C. Marquina, J. Blasco, J. Garcia, A. del Moral, and Z. Arnold, Nature (London), **386**, 256 (1997).
54. B. Batlogg, R. J. Cava, A. Jayaraman, R. B. van Dover, G. A. Kourouklis, S. Sunshine, D. W. Murphy, L. W. Rupp, H. S. Chen, A. White, K. T. Short, A. M. Muzsice, and E. A. Rietman, Phys. Rev. Lett. **58**, 2333 (1987).
55. L. C. Bourne, M. F. Crommie, A. Zettl, H. zur Loye, S. W. Keller, K. L. Leary, A. M. Stacy, K. J. Chang, M. L. Cohen, and D. E. Morris, Phys. Rev. Lett., **58**, 2337 (1987).
56. G. M. Zhao, K. K. Singh, and D. E. Morris, Phys. Rev. B **50**, 4112 (1994).
57. G. M. Zhao and D. E. Morris, Phys. Rev. B **51**, 16487R (1995).
58. G. M. Zhao, K. K. Singh, A. P. B. Sinha, and D. E. Morris, Phys. Rev. B **52**, 6840 (1995).
59. G. M. Zhao, M. B. Hunt, H. Keller, and K. A. Müller, Nature (London) **385**, 236 (1997).
60. G. M. Zhao, K. Conder, H. Keller, and K. A. Müller, J. Phys.: Condens. Matter, **10**, 9055 (1998).
61. R. J. McQueeney, Y. Petrov, T. Egami, M. Yethiraj, G. Shirane, and Y. Endoh, Phys. Rev. Lett. **82**, 628 (1999).

62. A. Lanzara, G. M. Zhao, N. L. Saini, A. Bianconi, K. Conder, H. Keller, and K. A. Müller, *J. Phys.: Condens. Matter* **11**, L541 (1999).
63. A. Shengelaya, G. M. Zhao, C. M. Aegerter, K. Conder, I. M. Savic, and H. Keller, *Phys. Rev. Lett.* **83**, 5142 (1999).
64. J. Hofer, K. Conder, T. Sasagawa, G. M. Zhao, M. Willemin, H. Keller, and K. Kishio, *Phys. Rev. Lett.* **84**, 4192 (2000).
65. G. M. Zhao, H. Keller, and K. Conder, *J. Phys.: Condens. Matter*, **13**, R569 (2001).
66. G. M. Zhao, *Phil. Mag. B* **81**, 1335 (2001).
67. G. M. Zhao, V. Kirtikar, and D. E. Morris, *Phys. Rev. B* **63**, 220506R (2001).
68. A. Lanzara *et al.*, *Nature (London)* **412**, 510(2001).
69. R. Khasanov *et al.*, *Phys. Rev. Lett.* **92**, 057602 (2004).
70. X. J. Zhou *et al.*, *Phys. Rev. Lett.* **95**, 117001 (2005).
71. G. M. Zhao, *Phys. Rev. B* **71**, 104517 (2005).
72. Z.-X. Shen, A. Lanzara, S. Ishihara, and N. Nagaosa, *Phil. Mag. B* **82**, 1349 (2002).
73. T. P. Devereaux, T. Cuk, Z.-X. Shen, and N. Nagaosa, *Phys. Rev. Lett.* **93**, 117004 (2004).
74. G. M. Zhao, *Phys. Rev. B* **64**, 024503 (2001); G. M. Zhao, *Phil. Mag. B* **84**, 3861 (2004); G. M. Zhao, *Phil. Mag. B* **84**, 3869 (2004).
75. B. H. Brandow, *Phys. Rev. B* **65**, 054503 (2002).
76. T. Thio *et al.*, *Phys. Rev. B* **38**, 905 (1988).
77. J. H. Cho, F. C. Chou, and D. C. Johnston, *Phys. Rev. Lett.* **70**, 222 (1993).
78. I. Eremin, O. Kamaev, and M. V. Eremin, *Phys. Rev. B* **69**, 094517 (2004).
79. X. X. Bi and P. C. Eklund, *Phys. Rev. Lett.* **70**, 2625 (1993).
80. O. Rösch *et al.*, *Phys. Rev. Lett.* **95**, 227002 (2005).
81. J. P. Carbotte, *Rev. Mod. Phys.* **62**, 1027 (1990).
82. P. D. Johnson, T. Valla, A.V. Fedorov, Z. Yusof, B. O. Wells, Q. Li, A. R. Moodenbaugh, G. D. Gu, N. Koshizuka, C. Kendziora, Sha Jian, and D. G. Hinks, *Phys. Rev. Lett.* **87**, 177007 (2001).
83. A. D. Gromko, A. V. Fedorov, Y.-D. Chuang, J. D. Koralek, Y. Aiura, Y. Yamaguchi, K. Oka, Yoichi Ando, and D. S. Dessau, *Phys. Rev. B* **68**, 174520 (2003).
84. H. Ding *et al.*, *Phys. Rev. Lett.* **74**, 2784 (1995).
85. R. S. Gonnelli, G. A. Ummarino, and V. A. Stepanov, *Physica C* **275**, 162 (1997).
86. W. E. Pickett, R. E. Cohen, and H. Krakauer, *Phys. Rev. Lett.* **67**, 228 (1991).
87. J. P. Carbotte, E. Schachinger, and D. N. Basov, *Nature (London)* **401**, 354 (1999).
88. E. Schachinger and J. P. Carbotte, *Phys. Rev. B*, **62**, 9054 (2000).
89. F. Marsiglio, T. Startseva, and J.P. Carbotte, *Physics Lett. A* **245**, 172 (1998).
90. J. Orenstein, *Nature (London)* **401**, 333 (1999).
91. V.M. Krasnov, A. Yurgens, D. Winkler, P. Delsing, and T. Claeson, *Phys. Rev. Lett.* **84**, 5860 (2000).
92. M. Opel *et al.*, *Phys. Rev. B* **60**, 9836 (1999).
93. C. O. Rodriguez, A. I. Liechtenstein, I. I. Mazin, O. Jepen, O. K. Anderson, M. methfessel, *Phys. Rev. B* **42**, 2692 (1990).
94. A. Abanov, A. V. Chubukov, and J. Schmalian, *Phys. Rev. B* **63**, 180510R (2001).